Earth Planet. Sci. Lett. 667 (2025) 119486

Contents lists available at ScienceDirect

Earth and Planetary Science Letters

journal homepage: www.elsevier.com/locate/epsl

Metallogeny of subduction initiation revealed by chalcophile element behaviour in the Samail ophiolite

Thomas M. Belgrano [a,b,*], James A. Milton [b], Larryn W. Diamond [c], Robin C. Wolf [c], Yuki Kusano [d], Damon A.H. Teagle [b]

[a] UCD School of Earth Sciences, University College Dublin, D04 N2E5, Ireland
[b] School of Ocean and Earth Science, National Oceanography Centre Southampton, University of Southampton, European Way, Southampton SO14 3ZH, UK
[c] Institute of Geological Sciences, University of Bern, Baltzerstrasse 3, 3012 Bern, Switzerland
[d] Geological Survey of Japan, National Institute of Advanced Industrial Science and Technology, Higashi 1-1-1, Tsukuba, Ibaraki 305-8567, Japan

ARTICLE INFO

Editor: Dr R. Hickey-Vargas

Keywords:
Gold
Ophiolite
VMS
Subduction initation
Oman

ABSTRACT

Intra-oceanic subduction initiation marks the transition between the mature divergent and convergent stages of the Wilson cycle, each with its relatively well understood metallogeny. The metallogenic systematics of this transition are less clear, however, with uncertainties regarding precious metal enrichment in volcanogenic massive sulfide (VMS) deposits and the potential for magmatic-hydrothermal mineralization in nascent arcs. The Samail ophiolite is increasingly accepted to represent a 'proto-arc' formed during subduction initiation. Due to its volcanic glass record of magmatism and resource estimates for its VMS deposits, this ophiolite is well suited for elucidating this metallogeny. New analyses of these volcanic glasses reveal a systematic enrichment in melt chalcophile elements over the course of ophiolite magmatism, with enrichment of Au > Cu ≈ Ag > Zn correlated with sulfide-melt affinity. This enrichment can be explained by sequential remelting of the proto-arc mantle, with initial melting concentrating Au into residual sulfide and later remelting extracting this Au into sulfide-undersaturated melts. Subsequent melt fractionation further increased Au/Cu ratios relative to sulfide-saturated early melts. Despite clear slab contamination, transfer of subducted S into the mantle was minimal. These observations demonstrate that tectono-magmatic evolution drives the coupled Au-enrichment of proto-arc lavas and the VMS deposits they host, with footwall lava composition controlling the metal endowment of these deposits. Despite H_2O-saturation of late boninitic melts, their low S contents and weak Cl fluid/melt partitioning inhibited magmatic-hydrothermal metal extraction, limiting potential for high-sulfidation mineralization. Subduction maturation is necessary to trigger such mineralization, as seen in Pacific intra-oceanic arc systems.

1. Introduction

In comparison to the mature divergent and convergent stages of the plate tectonic cycle, the metallogenic evolution of the subduction initiation stage that links them is relatively little explored (e.g., Patten et al., 2019; Valetich et al., 2018; Wang et al., 2021). Intra-oceanic subduction initiation commonly generates 'proto-arc' oceanic crust, formed by extension and magmatism above nascent subduction zones and commonly preserved as ophiolites and oceanic forearc sequences (e.g., Belgrano and Diamond, 2019; Shervais et al., 2019; Whattam and Stern, 2011). The characteristic shift from decompression-driven to slab-fluxed magmatism that occurs during formation of proto-arc crust suggests that chalcophile element behaviour should evolve over this process, providing an important record of the transition and controlling the distribution of metals within the crust. This is turn could impact the fertility and mineralization style of volcanogenic massive sulfide (VMS) ore systems (e.g., Furnes et al., 2022; Martin et al., 2019; Patten et al., 2017). However, understanding this evolution has proved challenging, because the requisite combination of a pristine magmatic record of subduction initiation with a corresponding metal inventory for sulfide deposits at different magmatic stages is rarely available.

The emerging accord that many supra-subduction zone ophiolites, including the Samail example (Oman–UAE), formed in proto-arc settings (Belgrano and Diamond, 2019; Whattam and Stern, 2011) necessitates revision of earlier views that their VMS districts are products of back-arc or mature fore-arc tectonics (Galley and Koski, 1997). While the details

* Corresponding author.
E-mail address: thomas.belgrano@ucd.ie (T.M. Belgrano).

https://doi.org/10.1016/j.epsl.2025.119486
Received 21 November 2024; Received in revised form 22 May 2025; Accepted 31 May 2025
Available online 24 June 2025

of the Samail ophiolite's tectonic origin will no doubt continue to be refined, its formation above a nascent subduction zone is supported by several independent strands of geochemical and geochronological evidence (e.g., Belgrano and Diamond, 2019; MacLeod et al., 2013; Rioux et al., 2021).

The recent discovery of volcanic glasses from all Samail volcanostratigraphic units (Belgrano et al., 2021; Kusano et al., 2017) together with volcanostratigraphic classification of their VMS ore resources (Cravinho et al., 2023; Gilgen et al., 2014) presents an opportunity to investigate the metallogenic evolution of subduction initiation and test metal sourcing models for mafic VMS systems. Motivation for understanding the polymetallic endowment of VMS deposits stems from their high Cu grades and Zn–Au–Ag(–Co–Se–Sb) co-production potential, which makes this deposit class attractive for minimizing the footprint and maximizing the return of extraction. A process-based metallogenic model for exploration of deposits with high co-production potential in ophiolites is currently lacking, however, and the potential for high sulfidation magmatic-hydrothermal mineralization in these settings remains unclear (e.g. Martin et al., 2021; Patten et al., 2017, 2019).

Gilgen et al. (2014) empirically showed that the first generation of VMS deposits in the Samail ophiolite tend to have the highest Cu grades in the sequence, whereas deposits hosted by later boninites have elevated Au grades. This systematic increase in deposit Au/Cu grade over the course of subduction initiation is a regional-scale pattern, suggesting that a fundamental yet unexplained process controls proto-arc VMS endowment. The possibility that Au was enriched by hydrothermal vent-site boiling at a shallower post-axial seafloor (Gilgen et al., 2014) is precluded by reconstructed pressure and temperature conditions outside the liquid–vapour stability field of seawater. These reconstructions combine paleobathymetric evidence for post-axial seafloor pressures >32 MPa (Belgrano et al., 2021) and fluid inclusion evidence for contemporary single-phase mineralizing fluids (Richter and Diamond, 2022). Key untested hypotheses remaining are additions of Au-rich magmatic-hydrothermal fluids (e.g., Patten et al., 2019) or hydrothermal leaching of Au-enriched footwall lavas (Cravinho et al., 2023; Gilgen et al., 2014; Patten et al., 2017).

This study tests these hypotheses via reconstruction of chalcophile element behaviour in the Samail VMS mineral system, integrating the results into a general model for the metallogenic evolution of subduction initiation. Building on studies focusing on the VMS deposit grade distribution and lava petrogenesis (Gilgen et al., 2014; Kusano et al., 2017; Belgrano et al., 2021) we present new analyses of the trace chalcophile element compositions of volcanic glasses for which major, volatile, and lithophile trace elements have already been partly reported (Belgrano et al., 2021; 2019; Kusano et al., 2017). Modelling of mantle melting and melt fractionation based on these glass compositions is then used to assess the relative importance of different chalcophile enrichment processes. Finally, the results are combined with existing VMS deposit data and the proto-arc model for ophiolite formation to build a process-based understanding of subduction initiation metallogeny.

1.1. Volcanostratigraphy, glass samples, and data

The magmatic evolution of the Samail ophiolite is recorded by its well-stratified volcanic sequence (Fig. 1a), with volcanostratigraphy and nomenclature recently reviewed by Belgrano et al. (2019). Initial tholeiitic magmatism proceeded at a proto-arc spreading axis, with the emplacement of 'moist' but otherwise mid-ocean ridge basalt (MORB)-like sheeted dike complex and comagmatic basaltic to andesitic 'Geotimes/V1' lavas (Kusano et al., 2012; MacLeod et al., 2013). Basalts of the 'Lasail/UV1' unit mostly overlie the axial crust discontinuously but constitute <10 area% of the lavas and hence are not considered in detail here (Belgrano et al., 2019). Post-axial, tholeiitic basalt–high-Mg-andesite–dacite–rhyolite series lavas of the 'Tholeiitic Alley/LV2' unit erupted almost ubiquitously over the axial crust, and their intrusive equivalents are present throughout the ophiolite (Belgrano et al., 2019; Haase et al., 2016; Kusano et al., 2014). Finally, post-axial, low silica boninite series lavas of the 'Boninitic Alley/UV2' unit erupted regionally but discontinuously with thicknesses up to ~2 km (Belgrano et al., 2019; Ishikawa et al., 2002; Kusano et al., 2014). The magmatic progression of the Samail ophiolite was halted at this point by obduction. Lavas with transitional compositions exist between most units and the timespan available for erupting the sequence is ~ 1 Myr (Rioux et al., 2021). The 18 Samail ophiolite VMS deposits with resource estimates lie mostly atop the axial volcanic crust and within the Boninitic Alley/UV2 lavas, but deposits exist at all levels (Fig. 1a; Gilgen et al., 2014).

Analyses of 53 volcanic glass samples are used in this study, with volcanostratigraphic affinity assigned according to previously defined compositional fields supported by volcanic map location (Figs. 1b, S1;

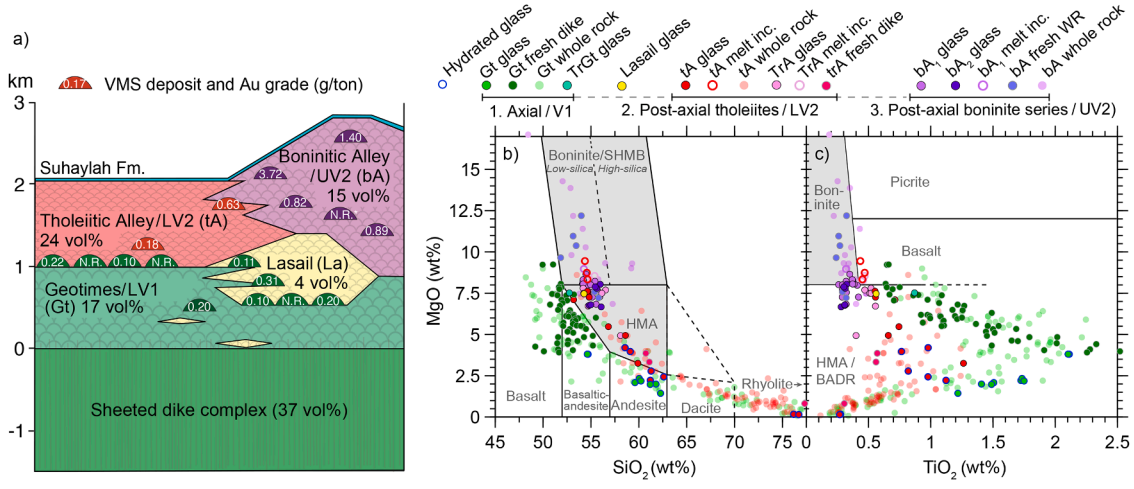

Fig. 1. Samail ophiolite upper crust and its volcanogenic massive sulfide (VMS) deposits. a) Volcanostratigraphy showing each of the Samail upper crustal units, with names (e.g. Geotimes) following Belgrano et al. (2019) and numbering (e.g., LV1) following Kusano et al. (2017), positions and Au grades of VMS deposits (Cravinho et al., 2023; Gilgen et al., 2014), and upper crustal volumes of each unit (Belgrano et al., 2019). b) and c) Lithologic classification of magmatic units based on MgO–TiO_2–SiO_2 relationships in fresh glass (Belgrano et al., 2021; 2019; Kusano et al., 2017), fresh dikes (Adachi and Miyashita, 2003; Miyashita et al., 2003), and variably altered lava and gabbro–plagiogranite whole rocks (Belgrano et al., 2019; Gilgen et al., 2016, 2014; Haase et al., 2016). Gt = Geotimes/V1, TrGt = Transitional V1/V2, tA = Tholeiitic Alley, TrA = Transitional Tholeiitic–Boninitic Alley, bA_{1-2} = Type 1–2 Boninitic Alley. Fields after Pearce and Reagan (2019)with HMA = High Mg Andesite and BADR = Basalt–Andesite–Dacite–Rhyolite series.

Belgrano et al., 2019). Glasses were recovered from pillow margins and hyaloclastite breccias (Belgrano et al., 2021; 2019; Kusano et al., 2017). Major, trace, and volatile element analyses previously reported in these studies have been collated here (Table A1, Belgrano et al., 2025). Pristine glasses are more common in the post-axial lavas and relict glass is exceedingly rare in the more hydrothermally altered axial sequence. The rarity of Geotimes/V1 glasses means that they are not evenly distributed across the compositional range of this unit, with most glasses being andesitic whereas most of the Geotimes/V1 dikes and lavas are basalts or basaltic andesites (Fig. 1b; Belgrano et al. 2019). All Geotimes/V1 glasses recovered so far appear to be affected by secondary devitrification and hydration (Fig. S4), as determined by electron microprobe analytical (EMPA) totals of 90–94 wt%. One key transitional Geotimes basalt glass is pristine (TB4–08D) and plots together with Geotimes/V1 geochemical arrays except for being slightly more depleted in incompatible lithophile elements. Data from glasses with secondary hydration are differentiated in our figures.

To support these glass data, X-ray fluorescence analyses of selected whole rock samples are included in our plots (File S1a). Petrographically, these samples are exceptionally fresh, they contain <2 wt% volatiles and closely follow primary MgO–SiO_2–CaO covariation curves. They include fresh axial sheeted dikes (Miyashita et al., 2003), Transitional Alley whole rock dikes (Adachi and Miyashita, 2003) and Boninitic Alley/UV2 pillow lavas (Ishikawa et al., 2002). Further use is made of published whole rock analyses of lavas, gabbros, and tonalites with <4 wt % volatiles which include Cu and Zn contents (File S1b; Belgrano et al., 2019; Belgrano and Diamond, 2019; Gilgen et al., 2014; Haase et al., 2016).

2. Analytical methods

A detailed record of analytical methods is provided in the supplement and summarised here. New major element, S, and Cl analyses of matrix glasses were performed by EMPA at the University of Bern using a Jeol JXA-8200™ instrument with a 15 keV, 30 nA and 15 μm diameter beam. Analyses of melt inclusions and their olivine hosts were performed with reduced current (20 nA) and beam size (5 μm) and corrected for post-entrapment crystallization using Petrolog (Danyushevsky and Plechov, 2011).

Conventional trace element compositions of volcanic glasses were determined by laser ablation inductively coupled plasma mass spectrometry (LA–ICP–MS) at the University of Bern using a Resonetics RESOlution SE 193 nm laser coupled to an Agilent 7900 ICP-MS. Basalt glass standard GSD-1G was used for calibration with SiO_2 determined by EMPA employed as an internal standard. Test analyses of MPI-DING glass reference materials compared well to reference values (Table A2; Belgrano et al., 2025) with all results for basalt glass ML3B-G within 10% of reference except for Ta, Cr, V (within 15%), Be, B, Cd, Sn, Sb (within 25%), and Ge, Cd (within 45–75%). Reference values for the latter groups have significant uncertainties. Median precision of replicate analyses of the Samail glasses expressed as% relative standard deviation (% RSD) was 2% for Cu, and 1% for Zn.

Concentrations of Au, Ag, As, and Pt in a subset of 34 glasses as well as Re in five glasses were determined by LA–ICP–MS at the University of Southampton by Agilent 8900 ICP-MS, using the ultra-low detection, interference-corrected Belgrano et al. (2022) method. Measured using San Carlos olivine blank material, the average 2σ lower limit of quantification for Au was 0.26 ng/g. With ThO/Th oxide production rates tuned to <0.08%, individual interference corrections for $^{181}Ta^{16}O$ and $^{180}Hf^{16}O^{1}H$ on ^{197}Au, $^{91}Zr^{16}O$ on ^{107}Ag, and $^{150}Sm^{++}$ and $^{150}Nd^{+}$ on ^{75}As amounted to <1% for Boninitic Alley/UV2 glasses, 1–10% for Tholeiitic Alley/LV2 glasses, 5–20% for mafic Geotimes/V1 glasses, and up to 25–40% for andesitic Geotimes/V1 glasses. Check analyses of basalt nano-powder pellet BIR-1-NP and NIST SRM616 were within 12% of preferred values for Au, 25% for Ag, 30% for Pt, and 10% for As (Belgrano et al., 2025). Median% RSD of replicate analyses of the Samail glasses was 9% for Au, 6% for Ag, 13% for Pt, and 3% for As.

2.1. Modelling methods

Major element compositions of the parental melts were calculated or assessed using PRIMELT3 (Herzberg and Asimow, 2015) via olivine addition (File S1f). A parental melt for Boninitic Alley/UV2 was modelled by adding 23 wt% olivine to the most primitive boninite glass composition (8.7 wt% MgO; OM17–62D; Kusano et al., 2017), such that melt MgO reached 17 wt%, matching the most primitive Boninitic Alley/UV2 whole rock (Belgrano et al., 2019) and in equilibrium with Fo_{94} olivine, consistent with Samail dunites (Rollinson, 2019). An 11.5 wt% MgO parental composition for Tholeiitic Alley/LV2 was calculated by adding 10 wt% olivine to glass TB4–12A (starting at 7.45 wt% MgO), to reach equilibrium with $Fo_{90.7}$ olivine in the LV2 residue (Kusano et al., 2017; Takazawa et al., 2003). A Geotimes/V1 parental melt composition was assumed equal to a 9.3 wt% MgO fresh dike whole rock with 0.91 wt% volatiles (96Om112; Miyashita et al., 2003), with this composition calculated to be in equilibrium with Fo_{91} olivine, higher than the $Fo_{90.4}$ axial residue olivine assumed by Kusano et al. (2017). Iron valency and H_2O were adjusted for different models and minor adjustments were made to Al_2O_3, TiO_2, and FeO_T concentrations to better intersect the glass arrays, correcting for minor spinel fractionation unaccounted for by olivine addition.

Rhyolite-MELTS v1.0.2 (Gualda et al., 2012) was used to model fractionation of the three main lava units (Fig. 2 and File S1c–e). Isobaric cooling models were run from the liquidus at 0.15 GPa for Geotimes and 0.12 GPa for the Alley magmas. These pressures correspond to depths of approximately 4.2 km and 3.2 km respectively, consistent with intrusive complexes in the ophiolite (Belgrano et al., 2019; Haase et al., 2016). Following initial tests (Fig. S2), fO_2 (in bar) was permitted to vary from an initial value of 0.5 log units above the fayalite–magnetite–quartz buffer (FMQ+0.5) for Geotimes/V1 and from FMQ+1 for Tholeiitic Alley/LV2. For Boninitic Alley/UV2, buffering at FMQ+2 produced the best results (Fig. 2c and S2). Rayleigh fractionation models for Au, Ag, Cu, and Zn melt evolution ignoring the possible effects of sulfide fractionation or degassing were calculated forwards and backwards through a primitive glass composition. These models were constructed by combining the MELTS phase proportions with compiled or calculated melt/mineral partition coefficients (Table S1) following Patten et al. (2019). Lithophile Zr fractionation was modelled in the same way to test the suitability of this approach (Fig. S3), as was Cl. Faithful reproduction of measured Zr arrays for each magmatic unit demonstrate the suitability of the approach.

Melt sulfide content at sulfide saturation ($SCSS_{2-}$) was calculated for Geotimes/V1 using both O'Neill (2021) and Li and Zhang (2022) models, the latter being H_2O-sensitive, utilizing physical and compositional parameters from the preferred MELTS models. The composition of a hypothetical segregated sulfide melt was calculated using the O'Neill (2021) model from Ni and Cu contents extrapolated from the measured glass compositions. Contributions of S^{6+} to total S solubility were accounted for according to Jugo et al. (2010) using fO_2 from the MELTS models, yielding total sulfur contents at sulfide saturation ($SCSS_T$) suitable for comparison to EMPA total S measurements. For reasons described by Wieser and Gleeson (2023), the Jugo et al. (2010) correction described above is invalid for the expectedly S^{6+}-dominated boninitic melts. Following their suggestion, a minor S^{2-} component calculated according to Li and Zhang (2022) was instead used to correct the sulfate content at anhydrite saturation ($SCAS_{6+}$) calculated after Chowdhury and Dasgupta (2019) to yield the total S content at anhydrite saturation ($SCAS_T$) for Boninitic Alley/UV2 melts.

Non-modal mantle fractional melting models were constructed for Cu, Ag, and Au following Lee et al. (2012). The Geotimes/V1 source was assumed to be depleted MORB mantle (DMM; Workman and Hart, 2005) following Belgrano and Diamond (2019), with 207 μg/g S, 27 μg/g Cu (Sun et al., 2020), 1.7 ng/g Au (Fischer-Gödde et al., 2011), 8 ng/g Ag

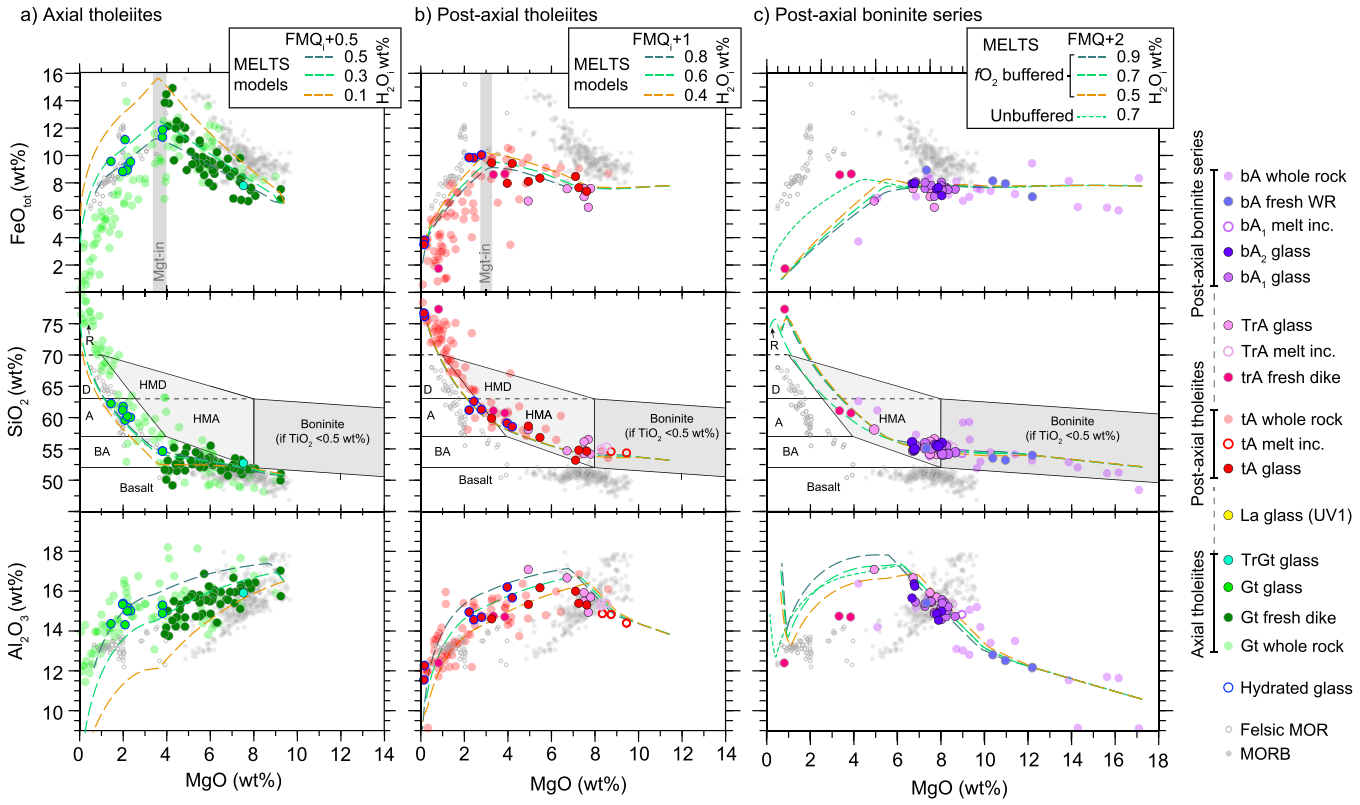

Fig. 2. Major element MgO–FeO_T–SiO_2–Al_2O_3 relationships in glass and whole rocks compared to MELTS models (all on an anhydrous basis) for the three regionally distributed Samail magmatic units. Data sources as for Fig. 1 for a) Axial tholeiites, b) Post-axial tholeiites, and c) Post-axial boninite series. Comparative MORB glasses from (Reekie et al., 2019) without back arc basalts and plume-influenced MORB). Felsic MOR andesite and dacite from Wanless et al. (2010) and Freund et al. (2013). Basalt, boninite, high-Mg andesite (HMA), basaltic andesite (BA), andesite (A), dacite (D), rhyolite (R) fields after Pearce and Reagan (2019). Rhyolite-MELTS models (Gualda et al., 2012) for various initial H_2O (H_2O_i) contents. Data symbols as Fig. 1.

(based on the Ag/Cu ratio of Wang and Becker, 2015), and 716 μg/g Ti. Fixed primary melt $SCSS_{2-}$ at source was calculated after Li and Zhang (2022) and sulfide partition coefficients after Li and Audetat (2015), assuming an upper mantle pressure of 0.5 GPa and the liquidus temperature, fO_2, and FeO_T for each unit's preferred MELTS starting composition (File S1). Chalcophile partition coefficients used for the silicate phases are listed in Table S1. Modal mineralogy for second and third stage melt sources were estimated by matching the modelled source TiO_2 with the mineralogy of depleted Samail lherzolites (Table S3; Takazawa et al., 2003).

3. Results

3.1. Major elements and fractionation modelling

Figs. 1b–c and 2 present a compilation of Samail glass compositions, with MgO as a monitor of magmatic fractionation. For the selected elements, there is fair correspondence between fresh materials and more scattered whole rocks, despite hydrothermal alteration of the latter. Geotimes/V1 glasses and fresh whole rocks follow common basalt–andesite–dacite–rhyolite (BADR) arrays with magnetite fractionation at ~3.5 wt% MgO, comparable to MORB but along slightly lower FeO_T and higher SiO_2–Al_2O_3 fractionation trajectories (Fig. 2a). Consistent with MacLeod et al. (2013), the Geotimes/V1 samples are best reproduced by MELTS models with initial water contents (0.3 wt%) slightly elevated relative to MORB, although scatter between the 0.1 to 0.5 wt% H_2O models.

Tholeiitic Alley/LV2 compositions range from basalt through high-Mg andesite to rhyolite, following lower but still tholeiitic FeO_T–TiO_2 trajectories relative to the axial melts, prior to the onset of magnetite fractionation at ~3 wt% MgO. The observed compositions are well bracketed by MELTS models starting with 0.4–0.8 wt% H_2O and logfO_2 at FMQ+1.

Boninitic Alley/UV2 compositions range from low-silica boninite to high-Mg andesite compositions with a flat FeO_T–TiO_2 evolution and high-Al_2O_3 trajectory up to ~6 wt% MgO, below which data are sparse (Fig. 1b and 2c). There is no clear separation between different groups of boninites in terms of the major elements. Observed compositions between 17 and 5 wt% MgO are well reproduced by the MELTS model with 0.7 wt% initial H_2O and logfO_2 buffered at FMQ+2, consistent with values of FMQ+1.8 determined from chromitites (Rollinson and Adetunji, 2015) and with shifts in EMPA *Kα* peak position suggesting S^{6+} dominated melts (see Supplement). Thus, the Samail melts became more hydrous and oxidized with time.

3.2. Base and precious metals

Concentrations of chalcophile elements Au, Ag, and Cu in the melts increased with each stage of Samail magmatism, in relative enrichment order Au > Ag ≈ Cu, whereas Zn behaved relatively conservatively (Fig. 3). Prior to magnetite fractionation, Geotimes/V1 melts had the lowest Au contents at 0.2–0.4 ng/g, overlapping with MORB (Fig. 3a). Tholeiitic Alley/LV2 glasses contain 2–3 ng/g Au and follow a relatively flat trajectory followed by depletion coincident with magnetite extraction. Post-axial Boninitic Alley/UV2 glasses have the highest measured Au contents (3–6 ng/g), 10–20x enriched over axial melts. Enrichment patterns for Ag are similar but notably scattered in the hydrated glasses, indicating low-temperature mobility. The behaviour of Cu shifts from progressive depletion in the axial melts to flat evolution in Tholeiitic Alley/LV2 melts to an enrichment trend in the boninite series melts.

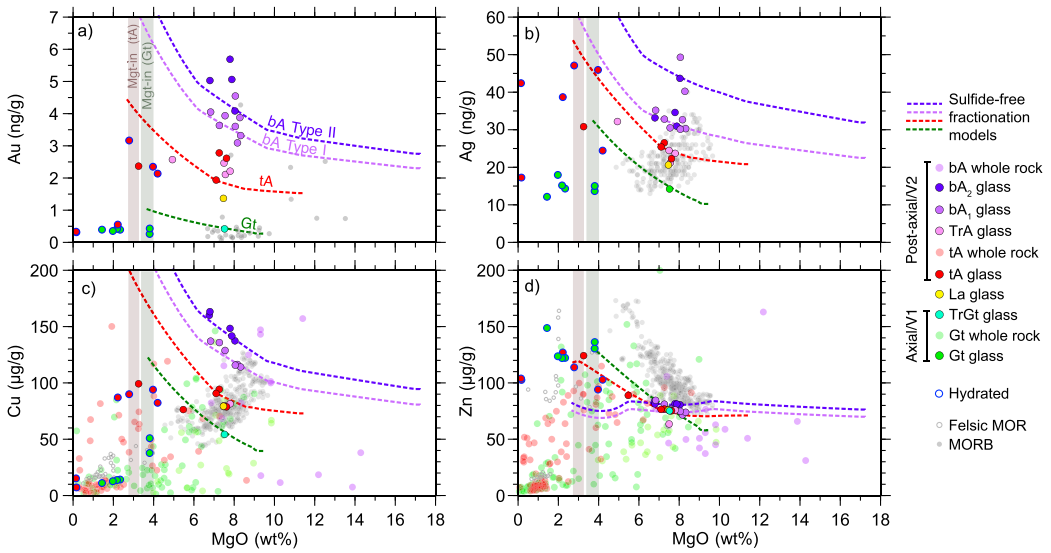

Fig. 3. Base and precious metal concentrations in Samail volcanic glasses as a function of melt fractionation monitored by MgO contents. a) Au, b) Ag, c) Cu, and d) Zn. Concentrations of Cu and Zn in variably altered whole rocks are shown for reference. Onsets of titanomagnetite fractionation (Fig. 2) are marked for Geotimes and Tholeiitic Alley. Comparative concentrations of Au in MORB are exclusively from ultra-low detection limit studies (Hertogen et al., 1980; Keays and Scott, 1976; Patten et al., 2015; Tatsumi et al., 1999). MORB and felsic MOR data sources as for Fig. 2. Hypothetical fractionation models which do not account for a fractionating sulfide phase are fixed through a primitive glass composition.

Copper and to a less clear extent Au further define two sub-parallel enrichment trends within Boninitic Alley, here termed Type I and II (Fig 3c). The increases in Au, Ag, and Cu contents upwards through the volcanostratigraphy are reversed for Zn (Fig 3d).

3.3. Trace elements, critical metals, volatiles

Enrichment patterns for variably lithophile, chalcophile, and fluid-mobile elements As, Sb, Bi, Pb, W, Pt, B, Mo (Fig. 4a–g) are similar to Au, Ag, and Cu. Elements As, Sb, and Bi are enriched by one to two orders of magnitude in the post-axial melts relative to the axial melts and together with Pb, W, B, and Mo clearly divide Type I and Type II

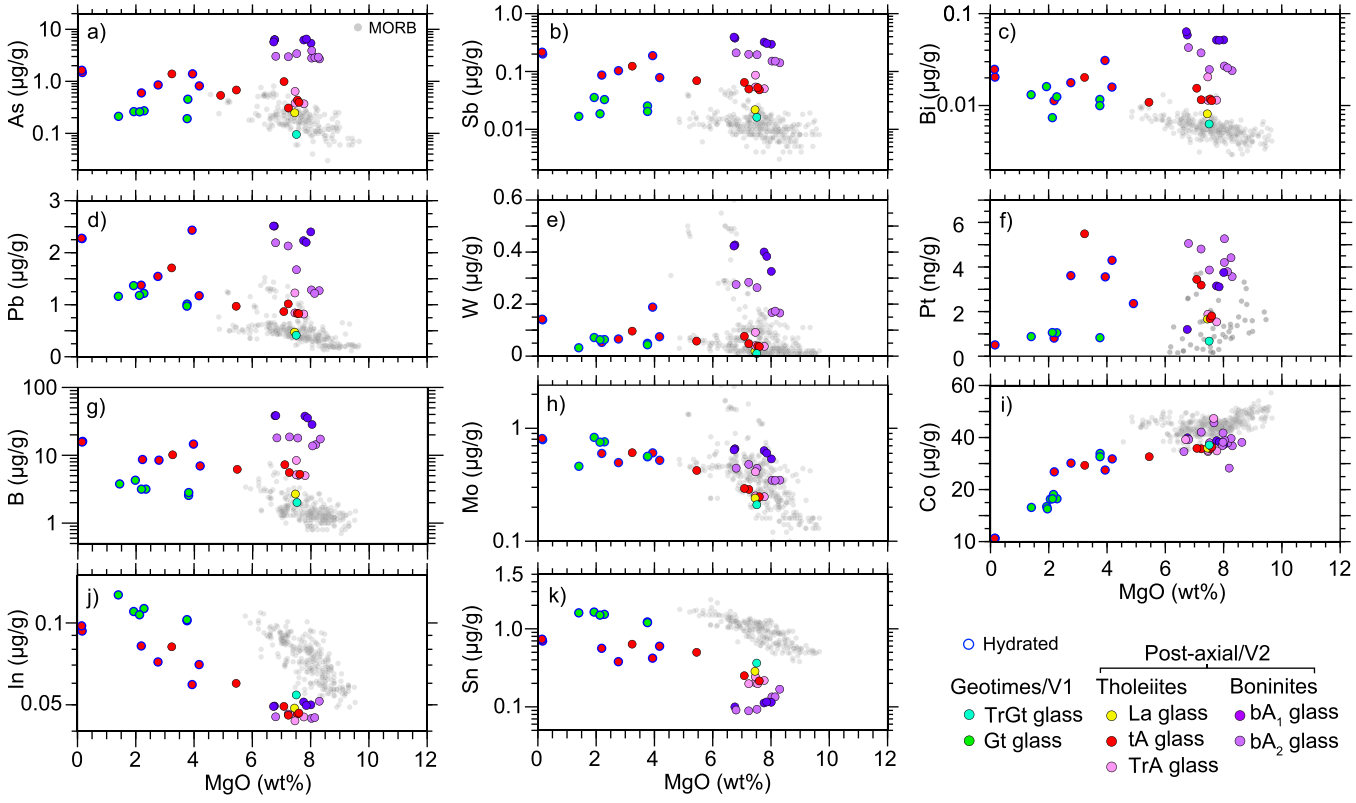

Fig. 4. Key trace element and critical metal concentrations during fractionation of Samail magmatic units, as monitored by MgO contents. Note both linear and log *y*-axes. MORB data source as for Fig. 2 except for B (Yang et al., 2018).

boninites. In the Geotimes/V1 glasses, concentrations of all these elements overlap with and disperse similarly to the MORB array. Like Zn, metals In and Sn exhibit reversed, increasingly depleted patterns (Fig. 4h–k), whereas Co follows a MORB-like depletion trend.

Concentrations of S in the axial Geotimes/V1 glasses (Fig. 5a) lie just below MORB values and close to the $SCSS_T$ models, although some perturbation by hydration is possible for the intermediate samples. Post-axial glasses and melt inclusions have <500 μg/g S, with scattered depletion trends and particularly low values for Boninitic Alley Type II glasses (~100–200 μg/g). Chlorine contents are elevated in the hydrated Geotimes/V1 glasses (1850–2450 μg/g). Considering only pristine glasses, Cl in the post-axial melts follows a similarly sloped but more enriched incompatible fractionation trajectory to MORB, from 200 to 300 μg/g Cl in melt inclusions to at least 560 μg/g in intermediate glasses (Fig. 5b).

4. Discussion

4.1. Effects of secondary glass devitrification and hydration

Owing to the rarity of glass in the Samail volcanic sequence, an adequate sample set can only be assembled by including some devitrified and weakly hydrated glasses (Fig. S4; Belgrano et al., 2021; Kusano et al., 2017). Only the freshest parts of these glasses were analysed, which are black and far fresher than other portions of the Samail outcrops, but typically have a subtly devitrified appearance under back-scattered electron imaging (Fig. S4), low EMPA totals, and molecular H_2O/OH^- ratios scattered above the values expected for pristine glass (Belgrano et al. 2021). Petrographically, this devitrification and hydration is distinct from and overprinted by metasomatic alteration along fractures (Fig. S4j–k).

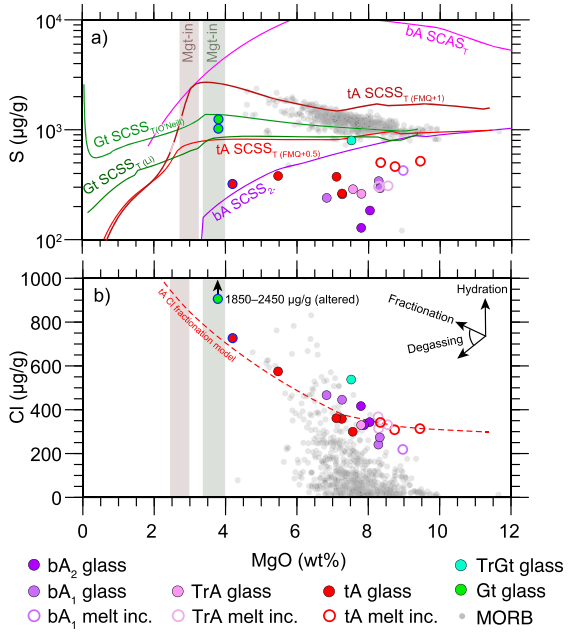

Fig. 5. Evolution of a) S and b) Cl in glass and melt inclusions during melt fractionation, as monitored by MgO contents. Total S content at sulfide saturation ($SCSS_T$) calculated for Geotimes/V1 (Gt) using both anhydrous (O'Neill, 2021) and hydrous (Li and Zhang, 2022) models, for Tholeiitic Alley/LV2 (tA) using just Li and Zhang (2022) with S^{6+} additions calculated after Jugo et al. (2010) for melts with initial fO_2 at FMQ+0.5 and +1. Boninitic Alley/UV2 S^{2-} content at sulfide saturation ($SCSS_{2-}$) modelled after Li and Zhang (2022) and compared to total S content at anhydrite saturation ($SCAS_T$) after Chowdhury and Dasgupta (2019) corrected for S^{2-}. MORB data source as for Fig. 2. Tholeiitic Alley Cl fractional crystallization model ignoring the possible effects of degassing calculated assuming perfect silicate incompatibility.

To assess the extent to which this hydration has affected element compositions utilized for this study versus simply diluted them, we consider whether elements plotted on an anhydrous basis fall within arrays defined by pristine glasses from the same unit in Figs. 1–3. For this test, trace element alteration would scatter compositions from the pristine array, whereas dilution would have little effect. The anhydrous compositions of the hydrated glasses plot concordantly with the pristine glasses for key elements Si, Mg, Al, Fe, Cu, and Au, demonstrating that hydration simply diluted these elements. Of the remaining elements most appear relatively unperturbed but this is difficult to assess for the rhyolite glasses. Concentrations of Cl, S, and Ag have been scattered during hydration. Users are therefore advised to these data with caution. Overall, the close correspondence between anhydrous concentrations of hydrated and pristine glasses for most elements and the petrographic distinction between early, relatively isochemical devitrification and later fracture-controlled alteration indicate that the concentrations of most elements in the hydrated glasses can be used judiciously.

4.2. Mechanisms of magmatic metal enrichment

Enrichment of economically important base and precious metals in supra-subduction zone magmas has previously been attributed to a variety of fractionation, source melting, and slab transfer processes (e.g., Jenner et al., 2010; Lee et al., 2012; Li et al., 2013; Patten et al., 2019, 2017), the contributions of which can all be effectively interrogated with our data.

4.3. Processes related to fractionation

Chalcophile element fractionation arrays of the Samail glasses characteristically progress from flat or depleting axial Geotimes/V1 trends to post-axial Boninitic Alley/UV2 enrichment trends (Fig. 3). To assess the influence of sulfide saturation state on these arrays (e.g., Jenner et al., 2010), sulfide-free fractional crystallization models are compared to the glass compositions. These show that Geotimes/V1 chalcophile elements evolved below the sulfide-free model curves, along sulfide-saturated trajectories comparable to MORB, but at somewhat lower concentrations, as best illustrated by Cu (Fig. 3c). Sulfur concentrations are similar to the two Geotimes/V1 $SCSS_T$ models (Fig. 5a), confirming that the Cu-depletion trend in these melts can be explained by Cu loss into a fractionating sulfide phase. Copper and Ag have similar sulfide melt / silicate melt partition coefficients ($D^{SulM/SilM}$) but Cu preferentially partitions into crystalline sulfide over Ag (Table A8; Li and Audétat, 2015). Constant Ag/Cu up to the onset of magnetite crystallization (Fig. 6a) shows this phase was a sulfide melt. Thereafter, increases in both Ag/Cu and Au/Cu are consistent with the onset of fractionation of a crystalline Cu-rich sulfide phase (Jenner et al., 2015, 2010).

Chalcophile elements in post-axial Tholeiitic Alley/LV2 melts evolve along relatively flat trends below sulfide-free trajectories, suggesting sulfide undersaturation (Fig. 3). Sulfide undersaturation of Tholeiitic Alley/LV2 melts is confirmed by glass and melt inclusion S contents well below the two $SCSS_T$ models (Fig. 5a) as well as by flat, albeit scattered, Au/Cu evolution over mafic to intermediate compositions (Fig. 6b). As $D^{SulM/SilM}$ for Au is typically ~10x greater than for Cu, the observed constancy of the ratio rules out sulfide melt segregation (Li and Audétat, 2015). Instead, this evidence points towards minor metal segregation into exsolving aqueous fluids. This interpretation is consistent with documented H_2O saturation (Belgrano et al., 2021), gentle S depletion (Fig 5a), and subtle depletion trends of high-fluid-affinity elements As, Sb, Bi, Pb, W, and B but not Pt between 4 and 2 wt% MgO in Fig. 4 (Audétat, 2019). This extraction was too inefficient to strongly deplete Cu and Au but buffered their concentrations during fractionation. In contrast, near-quantitative Cu–Au(–Pt–Co) depletion occurred at ~3 wt % MgO coincident with magnetite fractionation. As the high-fluid-affinity elements appear to maintain their concentrations,

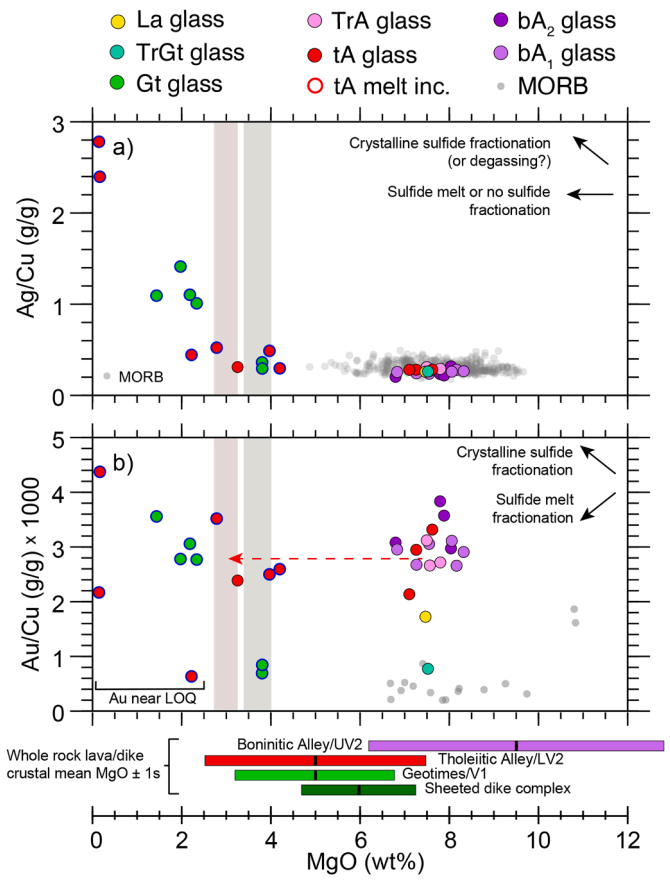

Fig. 6. Assessment of chalcophile enrichment/depletion mechanisms and precious/base metal ratios in Samail lavas with glass MgO versus a) Ag/Cu and b) Au/Cu. An indication of the approximate bulk composition of each VMS footwall unit is given by the mean ± 1 s MgO content of spilitic whole rock samples collected across the ophiolite and sheeted dike complex (Belgrano et al. 2019; Miyashita et al. 2003), ignoring the potential effects of alteration.

this Cu–Au(–Pt–Co) depletion is best explained by a magnetite-fractionation-induced sulfide saturation (e.g., Jenner et al., 2010) rather than by loss to exsolving magmatic-hydrothermal fluid (e.g., Patten et al., 2019).

For both Type I and II Boninitic Alley/UV2 glasses, Cu closely follows the sulfide-free fractionation models (Fig. 3), whereas Au and Ag are scattered around but not inconsistent with these models. These trajectories imply sulfide-undersaturated fractionation. Our glass analyses show that low primary S contents were principally responsible for tis sulfide undersaturation (Fig. 5a). Melt inclusions, hosted by olivine phenocrysts and likely trapped at depth, contain S well below the $SCSS_T$, showing that this low S cannot be due to simple seafloor degassing. In summary, fractionating sulfide melts preferentially stripped high $D^{SulM/SilM}$ metals from the axial Geotimes/V1 melts, whereas this process could not occur in the sulfide-undersaturated post-axial melts. This difference contributed to the increase in Au/Cu upwards through the Samail volcanostratigraphy.

4.4. Processes related to source melting

Simple fractional melting models constructed after Lee et al. (2012) are used to explore the effect of sequential mantle melting on primary chalcophile enrichment of proto-arc melts (Fig. 7). Such models are likely too simplistic to accurately reproduce this complex sequence (Wieser and Gleeson, 2023) and too few constraints on source composition and fO_2 are available to resolve this deficiency. However, the models serve to test the feasibility of a mantle control on the Samail chalcophile evolution (e.g., Hamlyn et al., 1985).

The upper row of Fig. 7 shows aggregate primary melt TiO_2 versus melt fraction (F). By assuming a DMM source for the first stage of melting and modelling melting until the target TiO_2 concentration in the primary melt for each lava unit is reached, estimates are obtained for F for each melt batch. These values are used to situate each melt extraction event on residue–melt models for Cu, Au, Ag, and S as a function of F in the lower rows of Fig. 7. Reproducing the Geotimes/V1 primary melt with 0.6 wt% TiO_2 requires 13 wt% melting of a DMM source, which depletes less than half of the original mantle sulfide (Fig. 7a). This residual sulfide buffers melt Au to low concentrations (<1 ng/g), with a similar but weaker effect on less chalcophile Ag and Cu. As residual sulfide persists at any reasonable degree of melting of the axial Geotimes/V1 source, or any typical modern MORB source, primary melts will always have low Au/Cu. Indeed, the model predicts an Au/Cu ratio essentially identical to the observed mean of the mafic axial glasses (8.0×10^{-6} versus 7.7×10^{-6} respectively). This confirmation rules out early Au-rich axial sulfide fractionation and the presence of a particularly Au-rich lower crustal cumulate reservoir in the ophiolite, despite no samples being available for this study to directly test this inference.

Modelling second-stage remelting of the Geotimes/V1 residue to target a Tholeiitic Alley/LV2 primary melt containing 0.45 wt% TiO_2 requires just ~3.4 wt% melting (Fig. 7b). The lower modal sulfide in the residue increases the amount of chalcophiles that dissolve in the second-stage melt. Nevertheless, second-stage residual sulfide persists up to a hypothetical melt degree of ~12 wt%, far beyond that indicated by the target TiO_2 value. In the third-stage melting model, the target Boninitic Alley/UV2 primary melt with 0.3 wt% TiO_2 is reached after melting ~5 wt% of the second-stage residue. Due to initially low modal sulfide abundance and complete consumption of free sulfide during this stage of melting, all modelled chalcophile elements in the silicate melts are elevated relative to previously extracted melts (Cu > 100 μg/g), broadly consistent with the observed glass compositions (Fig. 3). Exhaustion of the residual sulfide liberates Au that was pre-concentrated by earlier melt stages. With melting apparently terminating at this point, minor variations in the third stage melt degree would have sensitively controlled primary Au contents but would have affected Cu less, consistent with variable Au enrichment in the Boninitic Alley/UV2 glasses relative to Cu (Fig. 3).

The Samail proto-arc melting sequence could also be permissibly explained by other source compositions and sequences to that modelled in Fig. 7 (e.g., Kusano et al., 2017). For example, a DMM source that escaped axial melting would directly produce Tholeiitic Alley-like melts upon ~20 wt% melting, and Boninitic Alley-like melts could similarly be produced by higher degree melting of a first stage residue. However, due to the preferential extraction of S > Cu > Au prior to exhaustion of sulfide melt, these different sequences will all produce broadly similar results: post-axial melts depleted in S and enriched in chalcophile elements in order of their sulfide affinity. This interpretation explains the glass data well and is consistent with previous interpretations of chalcophile enrichment in similar boninitic magmas (Hamlyn et al., 1985; Valetich et al., 2018).

4.5. Enrichment by slab components

The models in Figs. 3 and 7 show that mantle re-melting and variations in sulfide saturation state during melt fractionation can readily explain the documented enrichment of chalcophile metals in the Samail post-axial lavas. Enrichments of Cu, Zn, and potentially Au in supra-subduction zone magmas have also been partly ascribed to additions of metal-enriched slab components (Furnes et al., 2022; Li et al., 2013). This could potentially be invoked to explain the parallel enrichment patterns of chalcophile elements and elements commonly transported in slab fluids (e.g., B, Cs, Li, As, and W; Fig. 4).

To assess the potential contribution of slab metals to proto-arc magmas, we compare experimental values of $D^{SulM/SilM}$ to a 'post-axial

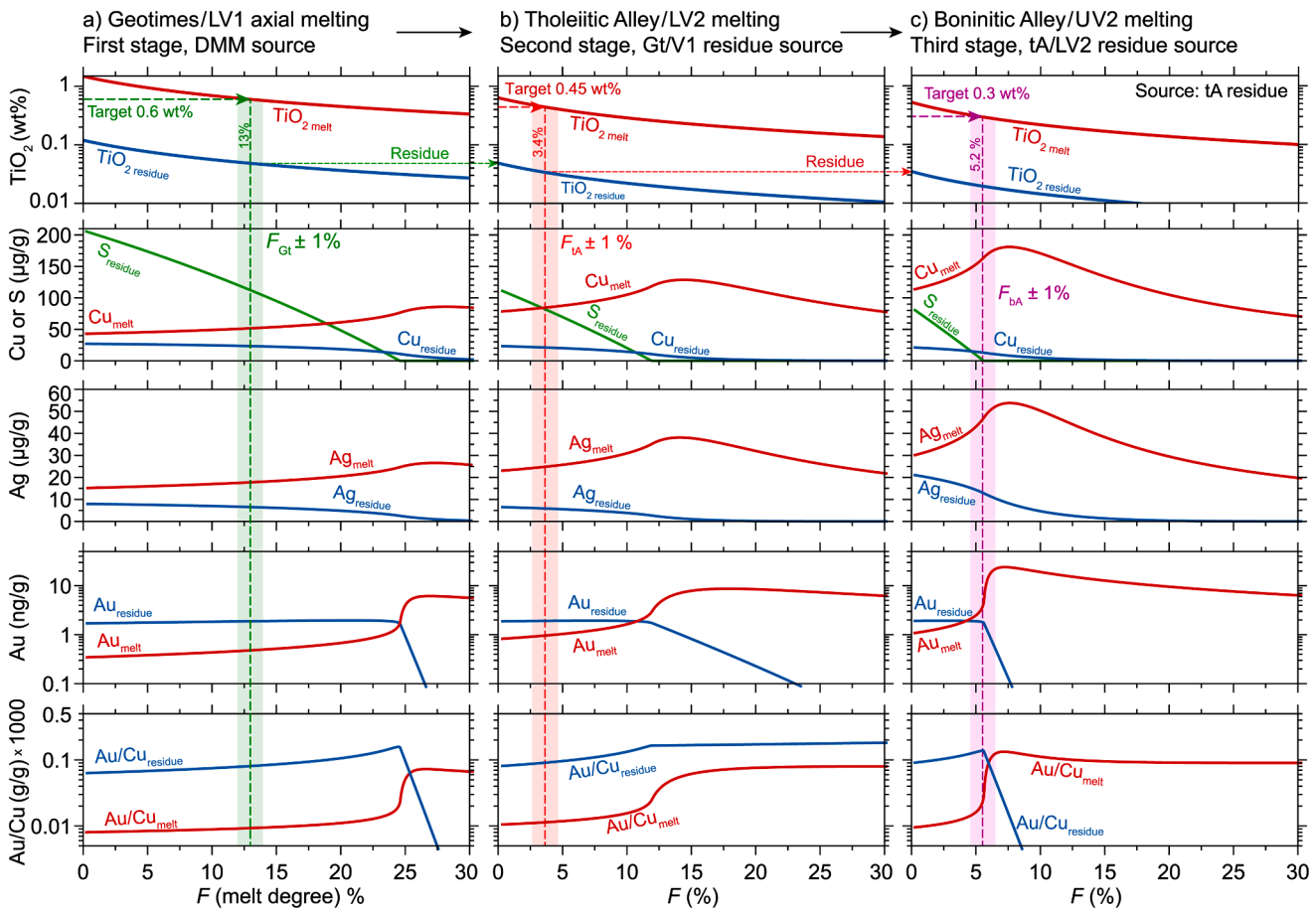

Fig. 7. Assessment of source related enrichment mechanisms with sequential mantle melting models adapted from Lee et al. (2012). Residue–melt models are shown for TiO_2 Cu, S, Ag, Au, and Au/Cu for a) Geotimes/V1 axial melts from a DMM source, b) Tholeiitic Alley/LV2 post-axial melts of the Geotimes/V1 residue, and c) Boninitic Alley/UV2 post-axial melts of the Tholeiitic Alley/LV2 residue. Shaded bands indicate melt degree (F, wt%) with an arbitrary ± 1% (absolute) uncertainty, estimated for each stage by targeting the TiO_2 calculated for each parental melt, as illustrated in the upper row.

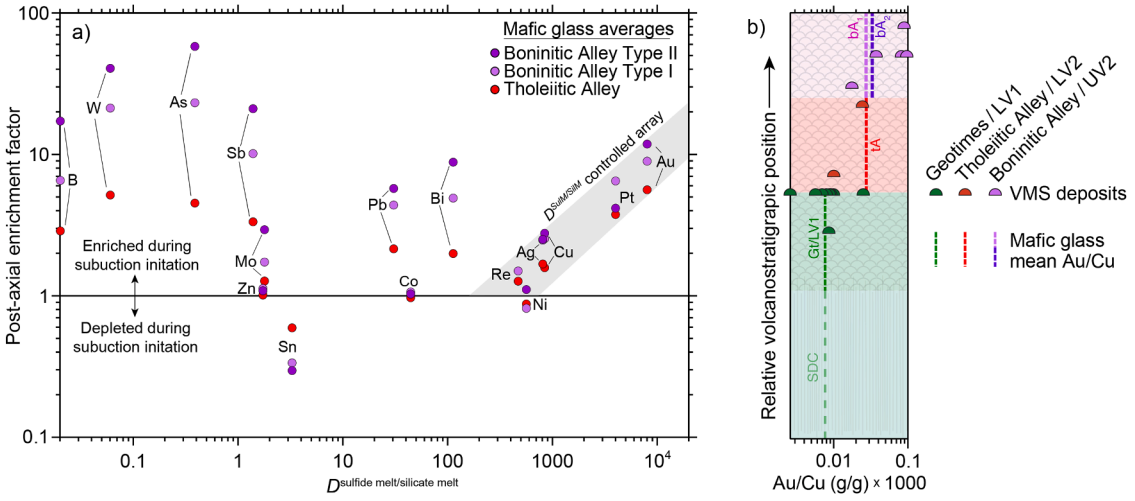

Fig. 8. Metal enrichment mechanisms and Samail Au/Cu ratios. a) Sulfide melt / silicate melt partition coefficients ($D^{SulM/SilM}$) versus enrichment factors for the post-axial glasses. $D^{SulM/SilM}$ calculated after Li and Audétat (2015) for a fixed 1270 °C, 7.5 wt% FeO_T, FMQ+1 post-axial melt, except for Pt and *Re* with MORB-mantle-like values of 4000 and 470, respectively (Feng and Li, 2019; Zhang and Li, 2021). Post-axial enrichment factor calculated from the mean mafic (>6 wt % MgO) glass compositions for each post-axial unit normalized to mafic axial glass TB4–08D b) Mean mafic glass Au/Cu ratios in each volcanostratigraphic unit (this study) compared to Au/Cu ratios of Samail ophiolite VMS deposits (Cravinho et al., 2023; Gilgen et al., 2014); relative volcanostratigraphic positions approximated from Gilgen et al. (2014) and the Belgrano et al. (2019) map.

enrichment factor', calculated from the mean composition of mafic glasses (>6 wt% $MgO_{anhydrous}$) in each post-axial unit normalized to axial mafic glass TB4–08D (Fig. 8a). As both the mantle re-melting and fractionation-related metal enrichment mechanisms discussed in the preceding two sections are controlled by affinity for immiscible sulphide melt, it follows that in the absence of additional processes, post-axial chalcophile enrichment should correlate directly with $D^{SulM/SilM}$ in each unit. Element enrichment above or to the left of this array would suggest slab derivation, whereas depletion below it would suggest loss to phases that fractionate to a greater extent in the post-axial melts (e.g., Cr-spinel, olivine, or perhaps aqueous fluid).

Chalcophile elements Re, Ag, Cu, Pt, and Au fall along a coherent enrichment array correlated with $D^{SulM/SilM}$, indicating that progressive enrichments of these metals in the Samail melts can indeed be explained by mantle remelting processes, somewhat amplified by fractionation processes, and that there is no requirement to invoke slab additions of these metals (Fig. 8a). Enrichments of elements plotting to the left of the $D^{SulM/SilM}$-controlled array (e.g., Bi, Pb, Sb, Mo, As, W, and B) in Fig. 8a are insufficiently chalcophile to be enriched by these mechanisms and must instead be slab derived, consistent with previous interpretations for some of these elements in Troodos lavas (Patten et al., 2017). Conservative behaviour or depletion of Zn, Sn, Co, and Ni is explained by their compatibility in olivine and spinel, with more extensive fractionation of these phases from the higher-*T*, more oxidized post-axial magmas.

4.6. Minimal transfer of proto-arc slab sulfur

The extent of slab-to-wedge transfer of S during subduction is of central importance to understanding subduction metallogeny (e.g., Li et al., 2020). Each melting episode in Oman became progressively depleted in S (Fig. 5a), despite being progressively enriched by slab-sediment-derived water and trace elements (Fig. 8a). This trend demonstrates that transfer of slab-derived S into the melting zone of the Samail mantle wedge was minimal. This accords with the observed behaviour of the chalcophile elements and S, which mimic melting models that do not consider effects of slab addition (Fig. 7). This conclusion is consistent with deductions of modest slab-to-wedge S transfer based on studies of blueschists and eclogites (e.g., Li et al., 2020), but it contrasts with the apparently high supply of slab-derived S required to produce S-rich, porphyry Cu-fertile magmas in arcs (e.g. Grondahl and Zajacz, 2022). It hence appears that transfer of slab S into the melting zone may increase as subduction zones mature, which would be an important factor controlling the onset of high sulfidation Cu–Au fertility in nascent arcs.

4.7. Controls on VMS Au enrichment

Gold enrichment of VMS ores has been documented in a variety of tectonic settings and adds economic value to otherwise base-metal-dominated deposits (e.g., Fuchs et al., 2019), including in the Samail ophiolite (Gilgen et al., 2014). With enhanced vent-site boiling ruled out as a mechanism to increase Au grades (Section 1), remaining potential causes of the selective Au enrichment of boninite-hosted VMS deposits in the ophiolite include elevated Au in the source rocks prior to hydrothermal leaching, the addition of Au-rich magmatic-hydrothermal fluids (e.g., Martin et al., 2021; Patten et al., 2019), and potentially obduction-related overprinting.

With obduction-related veins cutting the ophiolite (Belgrano et al., 2019), oveprinting by orogenic fluids could potentially be invoked as a Au enrichment mechanism in Oman. However, no such veins exist near most VMS deposits and where they do at the Geotimes/V1-hosted Hatta deposit, Au/Cu ratios are typical for the unit (Gilgen et al., 2014, 2016). Apart from these veins, the ophiolite upper crust has not experienced post-seafloor metamorphism (Belgrano et al., 2019). Hence, we rule out secondary overprinting as an Au enrichment mechanism.

A source rock compositional control on base and precious metal enrichment has been proposed for the Troodos ophiolite (Jowitt et al., 2012; Martin et al., 2019; Patten et al., 2017), although an unequivocal link for the precious metals has proved difficult to establish in the absence of Au data for different areas and generations of volcanics and VMS deposits. In the Samail ophiolite, the broad correlation of Au/Cu ratios in each generation of VMS deposits with those in their footwall units (Fig. 6b and 8b) provides clear evidence that hydrothermal leaching of subadjacent lavas is a control on Au contents in the deposits. This relationship is consistent with the matching footwall–ore REE patterns recognized in two post-axial deposits by Cravinho et al. (2023). Although elevated Au/Cu in andesitic Geotimes/V1 glasses (Fig. 6b) appears to contradict this conclusion, we recall that lavas with such compositions are volumetrically minor compared to mafic compositions, as shown by the mean MgO composition of the axial dikes and lavas (Fig. 6b). The axial upper crust subject to hydrothermal leaching is hence best represented by the glasses with >3 wt% MgO, which have low Au/Cu similar to the axial VMS deposits.

The close relationship with volcanic footwall composition shows that VMS-metal endowment dominantly reflects the composition of the upper km or so of crust below the contemporary seafloor horizon on which each VMS deposit is sitting (Fig. 1a). At least for the post-axial VMS deposits, this implies shallower hydrothermal metal leaching than typically envisaged for hydrothermal systems extracting metals from the sheeted dike complex (>2 km deep; Alt, 1997; Jowitt et al., 2012; Patten et al., 2017) or deeper in the crust (e.g., Jesus et al., 2025; Zihlmann et al., 2018), necessitating future consideration of the hydrothermal system structures (e.g., Fig. 9) and low-T metal solubilities required to explain this observation.

4.8. Potential for magmatic-hydrothermal Au enrichment

The Samail post-axial magmas were saturated in an H_2O-rich volatile phase and were rich in metals (Belgrano et al., 2021), but could magmatic-hydrothermal fluids have enriched Au in the boninite-hosted VMS deposits? We interpret the relatively flat evolution of Au and Cu in the sulfide-undersaturated Tholeiitic Alley/LV2 glass suite as evidence for partial magmatic-hydrothermal extraction of these elements. This process does not seem to have fractionated Au from Cu, however (Fig. 6b). Additionally, the absence of characteristic high-sulfidation, low pH hydrothermal alteration around post-axial intrusions and in VMS deposit feeder zones in Oman suggests the impact of magmatic fluids on VMS metallogeny was probably minimal, although not necessarily negligible (Cravinho et al., 2023; Richter and Diamond, 2022). The trace element evolution of the boninite series glasses does not support metal extraction into magmatic-hydrothermal fluids (Figs. 3 and 4). An association of Au with Sb–As enrichment in some boninite-hosted deposits would typically be interpreted as evidence of magmatic fluid input (Fuchs et al., 2019; Ixer et al., 1984; Martin et al., 2019). However, As and Sb enrichment is even greater than Au in the boninitic footwall rocks (Figs. 4, 8a). Invoking magmatic fluids is hence unnecessary to explain this association.

The question thus arises as to whether hydrous proto-arc magmas can produce 'hybrid' high sulfidation epithermal–VMS Cu–Au deposits at all (e.g., Fuchs et al., 2019; Martin et al., 2021). Slab-fluid-fluxed melting of proto-arc mantle produces Au-rich but S-poor melts and the mantle is not re-fertilized by slab S (Sect. 4.6). Magmatic S and Cl are essential ligands for the extraction and transport of Cu and Au from magmas into ore deposits (Grondahl and Zajacz, 2022). Low S contents in the Samail boninite melts would thus have suppressed the potential for magmatic–hydrothermal fluids to enrich VMS deposits in Au (or Cu). Chlorine reaches values of 500–700 μg/g at intermediate post-axial compositions (Fig. 5b). However, Cl fluid/melt partitioning reaches a minimum of ~2 at pressures and compositions corresponding to typical low pressure proto-arc melt fractionation (Botcharnikov et al., 2015). Extraction and transport of metals in chloride complexes would hence

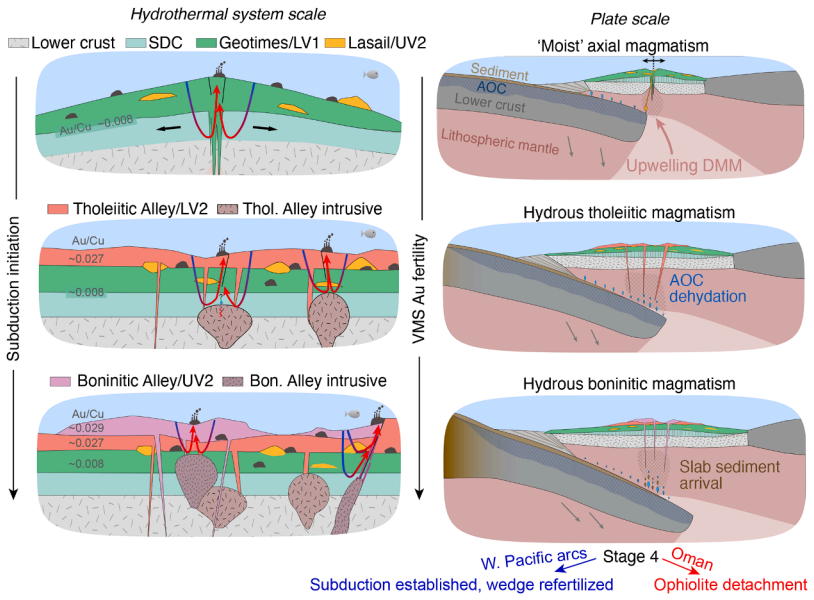

Fig. 9. A model for the coupled plate tectonic and metallogenic evolution of subduction initiation terranes as recorded by the Samail ophiolite, from plate to hydrothermal system scale. With potential high-level intrusive drivers of shallow post-axial hydrothermal circulation envisaged. Ratios of Au/Cu are in $g/g \times 1000$. Not to scale.

also have been minimized, as supported by the enrichment trend for Cl in the Samail post-axial melts despite evidence for H_2O loss (Fig. 6b; Belgrano et al., 2021).

The combination of minimal transfer of slab S, progressive depletion of S in the mantle wedge, and low pressure fractionation elucidate why proto-arc ophiolites that terminate their magmatic history with boninitic volcanism tend not to contain the high sulfidation mineralization common to intra-oceanic arc settings (e.g., de Ronde et al., 2011; Fuchs et al., 2019). Maturation of subduction, inducing mantle wedge re-fertilization with metals and S by mantle corner flow or slab metasomatism would be necessary to produce melts capable of more substantial magmatic-hydrothermal metallogenesis. This stage was not reached prior to detachment of the Samail and many other ophiolites (Whattam and Stern, 2011), unlike the many epithermal Au-mineralized intra-oceanic arcs and back-arcs in the SW Pacific (e.g., Palau, Vanuatu, Manus basin, Kermadec arc; de Ronde et al., 2011; Fuchs et al., 2019). Primary source-rock enrichments are instead a more probable driver of gold-enrichment in ophiolite-hosted VMS systems.

5. Conclusions

Analyses of up to 63 elements in a complete suite of Samail ophiolite glasses reveal that melts became progressively enriched in chalcophile elements during subduction initiation, in the order Au > Ag ≈ Cu > Zn, as controlled by sulfide melt affinity. The differential nature of this enrichment through time is largely explained by the sequential remelting of proto-arc mantle, which concentrated Au in residual sulfide melts, as initially suggested by Hamlyn et al. (1985). Source re-fertilization by slab S or metals was minimal, and subsequent post-axial sulfide-undersaturated magmatic fractionation amplified Au/Cu enrichment in comparison to earlier sulfide-saturated magmatic fractionation at the Samail spreading axis.

Fusing these interpretations of magmatic chalcophile behaviour with VMS deposit resource estimates and the proto-arc model for ophiolite petrogenesis leads to a general metallogenic model for the ophiolite and the subduction initiation stage that it records (Fig. 9). Metallogenesis evolved from formation of low Au/Cu VMS deposits at a proto-arc spreading axis to formation of elevated Au/Cu deposits during post-axial volcanism. This evolution was driven by the tectono-magmatic evolution of the ophiolite coupled with hydrothermal leaching of the progressively Au-enriched footwall rocks.

These findings can be applied as a VMS exploration guide, whereby boninitic sequences common in Precambrian to Phanerozoic ophiolite and greenstone terranes (Pearce and Reagan, 2019) should be prioritized for their higher Au potential, whereas typically earlier tholeiitic sequences should be prioritized for their higher Cu potential.

Finally, minimal slab S transfer, low melt S and weak Cl fluid/melt partitioning during magmatic fractionation suggest that economically significant magmatic-hydrothermal additions of Au and Cu to ore systems are inhibited at the proto-arc stage. Subduction zone maturation and wedge refertilization are necessary to trigger the onset of high sulfidation epithermal Au(-Cu) fertility in nascent arcs.

CRediT authorship contribution statement

Thomas M. Belgrano: Writing – original draft, Methodology, Investigation, Funding acquisition, Formal analysis, Conceptualization. **James A. Milton:** Writing – review & editing, Methodology. **Larryn W. Diamond:** Writing – review & editing, Resources, Conceptualization. **Robin C. Wolf:** Methodology, Investigation. **Yuki Kusano:** Writing – review & editing, Resources. **Damon A.H. Teagle:** Writing – review & editing, Supervision, Resources, Investigation.

Declaration of competing interest

The authors declare that they have no known competing financial interests or personal relationships that could have appeared to influence the work reported in this paper.

Acknowledgements

We thank the Ministry of Energy and Minerals (MEM), Sultanate of Oman, for their long support of our research into the Samail VMS systems and the team at National Earth Secrets Co. (Muscat) for logistical field support. The two reviewers are thanked for their suggestions, which substantially improved the manuscript, and Rosemary Hickey-Vargas is thanked for her editorial handling. We thank Lisa Richter, Sarah Pein, Samuel Weber, and Sam Pierre (all University of Bern) for assistance during field sampling and Samuel Gilgen and Penny Wieser for helpful discussions. Thomas Aebi kindly prepared glass mounts,

Pierre Lanari and Hugo Dominguez Carranza assisted with EMPA analysis, and Francesca Piccoli and Thomas Pettke with LA–ICP–MS analysis (all University of Bern). This research was supported by Swiss National Science Foundation (SNSF) grant no. 191795 to TMB, SNSF grant 169653 to LWD, and the Southampton Marine and Maritime Institute, University of Southampton.

Supplementary materials

Supplementary material associated with this article can be found, in the online version, at doi:10.1016/j.epsl.2025.119486.

Data availability

Data availability All new and compiled glass and analytical quality control data used in this study are provided in the linked permanent data archive: https://doi.org/10.5281/zenodo.15462896 (Belgrano et al., 2025).

References

Adachi, Y., Miyashita, S., 2003. Geology and petrology of the plutonic complexes in the Wadi Fizh area: multiple magmatic events and segment structure in the northern Oman ophiolite. Geochem. Geophys. Geosyst. 4. https://doi.org/10.1029/2001GC000272.

Alt, J.C., 1997. Hydrothermal Alteration and Mineralization of Oceanic Crust: Mineralogy, Geochemistry, and Processes. Society of Economic Geologists. Volcanic Associated Massive Sulfide Deposits: Processes and Examples in Modern and Ancient Settings.

Audétat, A., 2019. The metal content of magmatic-hydrothermal fluids and its relationship to mineralization potential. Econ. Geol. 114, 1033–1056. https://doi.org/10.5382/econgeo.4673.

Belgrano, T.M., Diamond, L.W., 2019. Subduction-zone contributions to axial volcanism in the Oman-U.A.E. ophiolite. Lithosphere 11, 399–411. https://doi.org/10.1130/L1045.1.

Belgrano, T.M., Diamond, L.W., Vogt, Y., Biedermann, A.R., Gilgen, S.A., Al-Tobi, K., 2019. A revised map of volcanic units in the Oman ophiolite: insights into the architecture of an oceanic proto-arc volcanic sequence. Solid Earth 10, 1181–1217. https://doi.org/10.5194/se-10-1181-2019.

Belgrano, T.M., Milton, J.A., Diamond, L.W., Wolf, R.C., Kusano, Y., Teagle, D.A.H., 2025. Data Archive for "Metallogeny of subduction initiation revealed by chalcophile element behaviour in the Samail ophiolite." https://doi.org/10.5281/zenodo.15462896.

Belgrano, T.M., Milton, J.A., Teagle, D.A.H., 2022. Determination of Ultra-Trace Au, Ag, As, Pt and *Re* mass fractions in volcanic glasses and rock powders by LA-ICP-MS. Geostand. Geoanal. Res. https://doi.org/10.1111/ggr.12452 n/a.

Belgrano, T.M., Tollan, P.M., Marxer, F., Diamond, L.W., 2021. Paleobathymetry of submarine lavas in the Samail and Troodos ophiolites: insights from volatiles in glasses and implications for hydrothermal systems. J. Geophys. Res. Solid Earth, e2021JB021966. https://doi.org/10.1029/2021JB021966 n/a.

Botcharnikov, R.E., Holtz, F., Behrens, H., 2015. Solubility and fluid–melt partitioning of H2O and Cl in andesitic magmas as a function of pressure between 50 and 500MPa. Chem. Geol. 418, 117–131. https://doi.org/10.1016/j.chemgeo.2015.07.019.

Chowdhury, P., Dasgupta, R., 2019. Effect of sulfate on the basaltic liquidus and Sulfur Concentration at Anhydrite Saturation (SCAS) of hydrous basalts – Implications for sulfur cycle in subduction zones. Chem. Geol. 522, 162–174. https://doi.org/10.1016/j.chemgeo.2019.05.020.

Cravinho, A., Jesus, A.P., Moreira, B., Mateus, A., Pracejus, B., Figueiras, J., Benoit, M., Bauer, W., Rocha, F., 2023. Contrasting Features and Volcanostratigraphy of the Mafic-Hosted Mandoos and Shinas Volcanogenic Massive Sulfide Deposits, 118. Economic Geology, Samail Ophiolite, Oman, pp. 1085–1124. https://doi.org/10.5382/econgeo.5006.

Danyushevsky, L.V., Plechov, P., 2011. Petrolog3: integrated software for modeling crystallization processes. Geochem. Geophys. Geosyst. 12. https://doi.org/10.1029/2011GC003516.

de Ronde, C.E.J., Massoth, G.J., Butterfield, D.A., Christenson, B.W., Ishibashi, J., Ditchburn, R.G., Hannington, M.D., Brathwaite, R.L., Lupton, J.E., Kamenetsky, V.S., Graham, I.J., Zellmer, G.F., Dziak, R.P., Embley, R.W., Dekov, V.M., Munnik, F., Lahr, J., Evans, L.J., Takai, K., 2011. Submarine hydrothermal activity and gold-rich mineralization at Brothers Volcano. Kermadec Arc, New Zealand. Miner Depos 46, 541–584. https://doi.org/10.1007/s00126-011-0345-8.

Feng, L., Li, Y., 2019. Comparative partitioning of *Re* and Mo between sulfide phases and silicate melt and implications for the behavior of *Re* during magmatic processes. Earth Planet. Sci. Lett. 517, 14–25. https://doi.org/10.1016/j.epsl.2019.04.010.

Fischer-Gödde, M., Becker, H., Wombacher, F., 2011. Rhodium, gold and other highly siderophile elements in orogenic peridotites and peridotite xenoliths. Chem. Geol. 280, 365–383. https://doi.org/10.1016/j.chemgeo.2010.11.024.

Freund, S., Beier, C., Krumm, S., Haase, K.M., 2013. Oxygen isotope evidence for the formation of andesitic–dacitic magmas from the fast-spreading Pacific–Antarctic Rise by assimilation–fractional crystallisation. Chem. Geol. 347, 271–283. https://doi.org/10.1016/j.chemgeo.2013.04.013.

Fuchs, S., Hannington, M.D., Petersen, S., 2019. Divining gold in seafloor polymetallic massive sulfide systems. Miner Depos 54, 789–820. https://doi.org/10.1007/s00126-019-00895-3.

Furnes, H., Dilek, Y., Kiseeva, E.S., 2022. Chalcophile element (Cu, Zn, Pb) and Ga distribution patterns in ancient and modern oceanic crust and their sources: petrogenetic modelling and a global synthesis. Gondwana Res. 109, 394–415. https://doi.org/10.1016/j.gr.2022.05.008.

Galley, A.G., Koski, R.A., 1997. Setting and characteristics of ophiolite-hosted volcanogenic massive sulfide deposits. Volcanic Associated Massive Sulfide Deposits: Processes and Examples in Modern Ancient Sett. https://doi.org/10.5382/Rev.08.10.

Gilgen, S.A., Diamond, L.W., Mercolli, I., 2016. Sub-seafloor epidosite alteration: timing, depth and stratigraphic distribution in the Semail ophiolite. Oman. Lithos 260, 191–210. https://doi.org/10.1016/j.lithos.2016.05.014.

Gilgen, S.A., Diamond, L.W., Mercolli, I., Al-Tobi, K., Maidment, D.W., Close, R., Al-Towaya, A., 2014. Volcanostratigraphic controls on the occurrence of massive sulfide deposits in the semail ophiolite. Oman. Economic Geology 109, 1585–1610. https://doi.org/10.2113/econgeo.109.6.1585.

Grondahl, C., Zajacz, Z., 2022. Sulfur and chlorine budgets control the ore fertility of arc magmas. Nat. Commun. 13, 4218. https://doi.org/10.1038/s41467-022-31894-0.

Gualda, G.A.R., Ghiorso, M.S., Lemons, R.V., Carley, T.L., 2012. Rhyolite-MELTS: a Modified Calibration of MELTS Optimized for Silica-rich, Fluid-bearing Magmatic Systems. J. Petrol. 53, 875–890. https://doi.org/10.1093/petrology/egr080.

Haase, K.M., Freund, S., Beier, C., Koepke, J., Erdmann, M., Hauff, F., 2016. Constraints on the magmatic evolution of the oceanic crust from plagiogranite intrusions in the Oman ophiolite. Contrib. Mineral. Petrol. 171, 1–16. https://doi.org/10.1007/s00410-016-1261-9.

Hamlyn, P.R., Keays, R.R., Cameron, W.E., Crawford, A.J., Waldron, H.M., 1985. Precious metals in magnesian low-Ti lavas: implications for metallogenesis and sulfur saturation in primary magmas. Geochim. Cosmochim. Acta 49, 1797–1811. https://doi.org/10.1016/0016-7037(85)90150-4.

Hertogen, J., Janssens, M.-J., Palme, H., 1980. Trace elements in ocean ridge basalt glasses: implications for fractionations during mantle evolution and petrogenesis. Geochim. Cosmochim. Acta 44, 2125–2143. https://doi.org/10.1016/0016-7037(80)90209-4.

Herzberg, C., Asimow, P.D., 2015. PRIMELT3 MEGA.XLSM software for primary magma calculation: peridotite primary magma MgO contents from the liquidus to the solidus. Geochem. Geophys. Geosyst. 16, 563–578. https://doi.org/10.1002/2014GC005631.

Ishikawa, T., Nagaishi, K., Umino, S., 2002. Boninitic volcanism in the Oman ophiolite: implications for thermal condition during transition from spreading ridge to arc. Geology 30, 899–902. https://doi.org/10.1130/0091-7613(2002)030<0899:BVITOO>2.0.CO;2.

Ixer, R.A., Alabaster, T., Pearce, J.A., 1984. Ore petrography and geochemistry of massive sulphide deposits within the Semail ophiolite, Oman. Transactions of the Institution of Mining and Metallurgy B 93, 114–124.

Jenner, F.E., Hauri, E.H., Bullock, E.S., König, S., Arculus, R.J., Mavrogenes, J.A., Mikkelson, N., Goddard, C., 2015. The competing effects of sulfide saturation versus degassing on the behavior of the chalcophile elements during the differentiation of hydrous melts. Geochemistry, Geophysics, Geosystems 16, 1490–1507. https://doi.org/10.1002/2014GC005670.

Jenner, F.E., O'Neill, H.S.T.C., Arculus, R.J., Mavrogenes, J.A., 2010. The magnetite crisis in the evolution of arc-related magmas and the initial concentration of Au, Ag and Cu. J. Petrol. 51, 2445–2464. https://doi.org/10.1093/petrology/egq063.

Jesus, A.P., Strauss, H., Gonçalves, M.A., Harris, M., Silva, D., Whitehouse, M.J., Teagle, D.A.H., 2025. Sulfur cycling in the gabbroic section of the Oman ophiolite. Lithos 494–495, 107913. https://doi.org/10.1016/j.lithos.2024.107913.

Jowitt, S.M., Jenkin, G.R.T., Coogan, L.A., Naden, J., 2012. Quantifying the release of base metals from source rocks for volcanogenic massive sulfide deposits: effects of protolith composition and alteration mineralogy. J. Geochem. Explor. 118, 47–59. https://doi.org/10.1016/j.gexplo.2012.04.005.

Jugo, P.J., Wilke, M., Botcharnikov, R.E., 2010. Sulfur K-edge XANES analysis of natural and synthetic basaltic glasses: implications for S speciation and S content as function of oxygen fugacity. Geochim. Cosmochim. Acta 74, 5926–5938. https://doi.org/10.1016/j.gca.2010.07.022.

Keays, R.R., Scott, R.B., 1976. Precious metals in ocean-ridge basalts; implications for basalts as source rocks for gold mineralization. Econ. Geol. 71, 705–720. https://doi.org/10.2113/gsecongeo.71.4.705.

Kusano, Y., Adachi, Y., Miyashita, S., Umino, S., 2012. Lava accretion system around mid-ocean ridges: volcanic stratigraphy in the Wadi Fizh area, northern Oman ophiolite. Geochemistry, Geophysics, Geosystems 13. https://doi.org/10.1029/2011GC004006.

Kusano, Y., Hayashi, M., Adachi, Y., Umino, S., Miyashita, S., 2014. Evolution of volcanism and magmatism during initial arc stage: constraints on the tectonic setting of the Oman Ophiolite. Geological Society, London 392, 177–193. https://doi.org/10.1144/SP392.9. Special Publications.

Kusano, Y., Umino, S., Shinjo, R., Ikei, A., Adachi, Y., Miyashita, S., Arai, S., 2017. Contribution of slab-derived fluid and sedimentary melt in the incipient arc magmas with development of the paleo-arc in the Oman Ophiolite. Chem. Geol. 449, 206–225. https://doi.org/10.1016/j.chemgeo.2016.12.012.

Lee, C.-T.A., Luffi, P., Chin, E.J., Bouchet, R., Dasgupta, R., Morton, D.M., Le Roux, V., Yin, Q., Jin, D., 2012. Copper Systematics in Arc Magmas and Implications for Crust-Mantle Differentiation. Science 336 (1979), 64–68. https://doi.org/10.1126/science.1217313.

Li, H., Zhang, L., 2022. A thermodynamic model for sulfur content at sulfide saturation (SCSS) in hydrous silicate melts: with implications for arc magma genesis and sulfur recycling. Geochim. Cosmochim. Acta 325, 187–204. https://doi.org/10.1016/j.gca.2022.03.008.

Li, J.-L., Gao, J., John, T., Klemd, R., Su, W., 2013. Fluid-mediated metal transport in subduction zones and its link to arc-related giant ore deposits: constraints from a sulfide-bearing HP vein in lawsonite eclogite (Tianshan, China). Geochim. Cosmochim. Acta 120, 326–362. https://doi.org/10.1016/j.gca.2013.06.023.

Li, J.-L., Schwarzenbach, E.M., John, T., Ague, J.J., Huang, F., Gao, J., Klemd, R., Whitehouse, M.J., Wang, X.-S., 2020. Uncovering and quantifying the subduction zone sulfur cycle from the slab perspective. Nat. Commun. 11, 514. https://doi.org/10.1038/s41467-019-14110-4.

Li, Y., Audétat, A., 2015. Effects of temperature, silicate melt composition, and oxygen fugacity on the partitioning of V, Mn, Co, Ni, Cu, Zn, As, Mo, Ag, Sn, Sb, W, Au, Pb, and Bi between sulfide phases and silicate melt. Geochim. Cosmochim. Acta 162, 25–45. https://doi.org/10.1016/j.gca.2015.04.036.

MacLeod, C.J., Johan Lissenberg, C., Bibby, L.E., 2013. Moist MORB" axial magmatism in the Oman ophiolite: the evidence against a mid-ocean ridge origin. Geology 41, 459–462. https://doi.org/10.1130/G33904.1.

Martin, A.J., Keith, M., McDonald, I., Haase, K.M., McFall, K.A., Klemd, R., MacLeod, C. J., 2019. Trace element systematics and ore-forming processes in mafic VMS deposits: evidence from the Troodos ophiolite. Cyprus. Ore Geol. Rev. 106, 205–225. https://doi.org/10.1016/j.oregeorev.2019.01.024.

Martin, A.J., McDonald, I., Jenkin, G.R.T., McFall, K.A., Boyce, A.J., Jamieson, J.W., MacLeod, C.J., 2021. A missing link between ancient and active mafic-hosted seafloor hydrothermal systems – Magmatic volatile influx in the exceptionally preserved Mala VMS deposit, Troodos, Cyprus. Chem. Geol. 567, 120127. https://doi.org/10.1016/j.chemgeo.2021.120127.

Miyashita, S., Adachi, Y., Umino, S., 2003. Along-axis magmatic system in the northern Oman ophiolite: implications of compositional variation of the sheeted dike complex. Geochemistry, Geophysics, Geosystems 4. https://doi.org/10.1029/2001GC000235.

O'Neill, H.St.C., 2021. The thermodynamic controls on sulfide saturation in silicate melts with application to ocean floor basalts. Magma Redox Geochemistry. Geophysical Monograph Series, pp. 177–213. https://doi.org/10.1002/9781119473206.ch10.

Patten, C.G.C., Pitcairn, I.K., Alt, J.C., Zack, T., Lahaye, Y., Teagle, D.A.H., Markdahl, K., 2019. Metal Fluxes During Magmatic Degassing in the Oceanic crust: Sulfide Mineralisation At ODP Site 786B, Izu-Bonin forearc. Miner Depos. https://doi.org/10.1007/s00126-019-00900-9.

Patten, C.G.C., Pitcairn, I.K., Teagle, D.A.H., 2017. Hydrothermal mobilisation of Au and other metals in supra-subduction oceanic crust: insights from the Troodos ophiolite. Ore Geol. Rev. https://doi.org/10.1016/j.oregeorev.2017.02.019.

Patten, C.G.C., Pitcairn, I.K., Teagle, D.A.H., Harris, M., 2015. Mobility of Au and related elements during the hydrothermal alteration of the oceanic crust: implications for the sources of metals in VMS deposits. Miner Depos 51, 179–200. https://doi.org/10.1007/s00126-015-0598-8.

Pearce, J.A., Reagan, M.K., 2019. Identification, classification, and interpretation of boninites from Anthropocene to Eoarchean using Si-Mg-Ti systematics. Geosphere. https://doi.org/10.1130/GES01661.1.

Reekie, C.D.J., Jenner, F.E., Smythe, D.J., Hauri, E.H., Bullock, E.S., Williams, H.M., 2019. Sulfide resorption during crustal ascent and degassing of oceanic plateau basalts. Nat. Commun. 10, 82. https://doi.org/10.1038/s41467-018-08001-3.

Richter, L., Diamond, L.W., 2022. Characterization of hydrothermal fluids that alter the upper oceanic crust to spilite and epidosite: fluid inclusion evidence from the Semail (Oman) and Troodos (Cyprus) ophiolites. Geochim. Cosmochim. Acta 309, 220–253. https://doi.org/10.1016/j.gca.2021.11.012.

Rioux, M., Garber, J.M., Searle, M., Kelemen, P., Miyashita, S., Adachi, Y., Bowring, S., 2021. High-precision U-Pb zircon dating of late magmatism in the Samail ophiolite: a record of subduction initiation. J. Geophys. Res. Solid Earth, e2020JB020758. https://doi.org/10.1029/2020JB020758 n/a.

Rollinson, H., 2019. Dunites in the mantle section of the Oman ophiolite – The boninite connection. Lithos 334–335, 1–7. https://doi.org/10.1016/j.lithos.2019.03.008.

Rollinson, H., Adetunji, J., 2015. The geochemistry and oxidation state of podiform chromitites from the mantle section of the Oman ophiolite: a review. Gondwana Res. 27, 543–554. https://doi.org/10.1016/j.gr.2013.07.013.

Shervais, J.W., Reagan, M., Haugen, E., Almeev, R., Pearce, J., Prytulak, J., Ryan, J.G., Whattam, S., Godard, M., Chapman, T., Li, H., Kurz, W., Nelson, W.R., Heaton, D., Kirchenbaur, M., Shimizu, K., Sakuyama, T., Li, Y., Vetter, S.K., 2019. Magmatic Response to Subduction Initiation, Part I: Forearc basalts of the Izu-Bonin Arc from IODP Expedition 352. Geochem. Geophys. Geosyst. 20, 314–338. https://doi.org/10.1029/2018GC007731.

Sun, Z., Xiong, X., Wang, J., Liu, X., Li, L., Ruan, M., Zhang, L., Takahashi, E., 2020. Sulfur abundance and heterogeneity in the MORB mantle estimated by copper partitioning and sulfur solubility modelling. Earth Planet. Sci. Lett. 538, 116169. https://doi.org/10.1016/j.epsl.2020.116169.

Takazawa, E., Okayasu, T., Satoh, K., 2003. Geochemistry and origin of the basal lherzolites from the northern Oman ophiolite (northern Fizh block). Geochemistry, Geophysics, Geosystems 4. https://doi.org/10.1029/2001GC000232.

Tatsumi, Y., Oguri, K., Shimoda, G., 1999. The behaviour of platinum-group elements during magmatic differentiation in Hawaiian tholeiites. Geochem. J. 33, 237–247. https://doi.org/10.2343/geochemj.33.237.

Valetich, M.J., Mavrogenes, J., Arculus, R., Umino, S., 2018. Evolution of chalcophile elements in the magmas of the Bonin Islands. Chem. Geol. https://doi.org/10.1016/j.chemgeo.2018.07.011.

Wang, Z., Becker, H., 2015. Abundances of Ag and Cu in mantle peridotites and the implications for the behavior of chalcophile elements in the mantle. Geochim. Cosmochim. Acta 160, 209–226. https://doi.org/10.1016/j.gca.2015.04.006.

Wang, Z., Zhang, P., Li, Y., Ishii, T., Li, W., Foley, S., Wang, Xiang, Wang, Xia, Li, M., 2021. Copper recycling and redox evolution through progressive stages of oceanic subduction: insights from the Izu-Bonin-Mariana forearc. Earth Planet. Sci. Lett. 574, 117178. https://doi.org/10.1016/j.epsl.2021.117178.

Wanless, V.D., Perfit, M.R., Ridley, W.I., Klein, E., 2010. Dacite petrogenesis on mid-ocean ridges: evidence for oceanic crustal melting and assimilation. J. Petrol. https://doi.org/10.1093/petrology/egq056.

Whattam, S.A., Stern, R.J., 2011. The "subduction initiation rule": a key for linking ophiolites, intra-oceanic forearcs, and subduction initiation. Contrib. Mineral. Petrol. 162, 1031–1045. https://doi.org/10.1007/s00410-011-0638-z.

Wieser, P., Gleeson, M., 2023. PySulfSat: an open-source Python3 tool for modeling sulfide and sulfate saturation. Volcanica 6, 107–127. https://doi.org/10.30909/vol.06.01.107127.

Workman, R.K., Hart, S.R., 2005. Major and trace element composition of the depleted MORB mantle (DMM). Earth Planet. Sci. Lett. 231, 53–72. https://doi.org/10.1016/j.epsl.2004.12.005.

Yang, S., Humayun, M., Salters, V.J.M., 2018. Elemental Systematics in MORB Glasses From the Mid-Atlantic Ridge. Geochem. Geophys. Geosyst. 19, 4236–4259. https://doi.org/10.1029/2018GC007593.

Zhang, M., Li, Y., 2021. Breaking of Henry's law for sulfide liquid–basaltic melt partitioning of Pt and Pd. Nat. Commun. 12, 5994. https://doi.org/10.1038/s41467-021-26311-x.

Zihlmann, B., Müller, S., Coggon, R.M., Koepke, J., Garbe-Schönberg, D., Teagle, D.A.H., 2018. Hydrothermal fault zones in the lower oceanic crust: an example from Wadi Gideah, Samail ophiolite. Oman. Lithos 323, 103–124. https://doi.org/10.1016/j.lithos.2018.09.008.